

Direct observation of coherent energy transfer in nonlinear micro-mechanical oscillators

Changyao Chen¹, Damián H. Zanette², David Czaplewski¹, Steven Shaw³, and Daniel López^{1*}

¹*Center for Nanoscale Materials, Argonne National Laboratory, 9700 South Cass Avenue, Argonne, IL 60439*

²*Centro Atómico Bariloche and Instituto Balseiro, Comisión Nacional de Energía Atómica. Consejo Nacional de Investigaciones Científicas y Técnicas. 8400 San Carlos de Bariloche, Río Negro, Argentina.*

³*Department of Mechanical and Aerospace Engineering, Florida Institute of Technology, 150 West University Blvd., Melbourne, FL 32901*

* *Corresponding email: dlopez@anl.gov*

Energy dissipation is an unavoidable phenomenon of physical systems that are directly coupled to an external environmental bath. The ability to engineer the processes responsible for dissipation and coupling is fundamental to manipulate the state of such systems^{1,2}. This is particularly important in oscillatory states whose dynamic response is used for many applications, e.g. micro and nano-mechanical resonators for sensing^{3,4} and timing^{5,6}, qubits for quantum engineering⁷, and vibrational modes for optomechanical devices⁸. In situations where stable oscillations are required, the energy dissipated by the vibrational modes is usually compensated by replenishment from external energy sources. Consequently, if the external energy supply is removed, the amplitude of oscillations start to decay immediately, since

there is no means to reconstitute the energy dissipated. Here, we demonstrate a novel strategy to maintain stable oscillations, i.e. with constant amplitude and frequency, without supplying external energy to compensate losses. The fundamental intrinsic mechanism of resonant mode coupling is used to redistribute and store mechanical energy among vibrational modes and coherently transfer it back to the principal mode when the external excitation is off. To experimentally demonstrate this phenomenon that defies physical intuition, we exploit the nonlinear dynamic response of microelectromechanical (MEMS) oscillators to couple two different vibrational modes through an internal resonance⁹. Since the underlying mechanism describing the fundamentals of this new phenomenon is generic and representative of a large variety of systems, the presented method provides a new dissipation engineering strategy that would enable a new generation of autonomous devices.

Micro and nano-scale mechanical resonators are examples of oscillatory systems that have been studied for decades, since they offer great flexibility to design their mechanical response and their intrinsic and extrinsic dissipation mechanisms^{10,11}. For instance, expeditious energy dissipation is required in applications such as vibration isolation or switching, where mechanical motions need to be quickly damped out^{12,13}. Conversely, small dissipation rates - or, equivalently, efficient isolation of the system of interest from its environment - are highly desired in other applications because they directly provide more stable frequency sources⁶, enhanced detection of extremely weak forces¹⁴, and allow for room-temperature quantum-coherent operations and sensing¹⁵⁻¹⁷. The goal of dissipation engineering is to control the dissipative processes in which the energy stored in the system can be guided towards the natural environment or another resonant mode in a predefined

manner. If the interaction with the other modes –such as an electromagnetic cavity^{18,19}, a light field²⁰, a phononic crystal²¹ or a mechanical vibration²²– is stronger than the interaction with the thermal bath, a new regime emerges as the system dynamics can be designed to enable distinctive behaviors. Most commonly, parametric modulation is used to activate and control the interaction, where an *external* modal control is applied to mediate the dynamics. Although parametric modulation can couple any two modes without any prerequisite relationship of their frequencies^{18,22}, hence capable of bridging distinct domains (e.g. optical modes in THz range, electrical modes in GHz range, and mechanical below MHz), the disparate frequencies typically make it difficult to achieve strong intermodal coupling. Here, we introduce a general mechanism that naturally couples mechanical modes with an intermodal coupling rate that greatly exceeds the intrinsic relaxation rate of the coupled modes. This is achieved by coupling different vibrational modes of a single oscillator through an internal resonance. Internal resonance²³ (IR) capitalizes on the condition where the resonant frequencies of two distinct modes satisfy a commensurate relationship to enable strong coupling and efficient energy transfer²⁴. Operating micromechanical oscillators in the nonlinear regime, where the resonant frequency has a strong dependence on the oscillation amplitude, allows for precise tuning of the principal mode oscillation frequency just by increasing the applied driving force and thus it can be used to access the IR condition. At IR, energy initially imparted to the principal mode will be continuously exchanged between all the resonantly coupled modes and, if the energy supply is turned off, this energy will be coherently redirected toward the principal mode, effectively keeping the principal mode of the resonator oscillating. Although IR holds great promise in areas such as frequency stabilization⁹ and energy harvesting^{25,26}, it has

never been utilized to engineer dissipation processes in micro and nano-resonators, partly because of the lack of definitive experimental results revealing the details of the energy transfer mechanism.

Clamped-clamped (c-c) beam resonators are the most common and popular type used in MEMS and nanoelectromechanical (NEMS) devices: they are straightforward to fabricate at the micro and nano-scale, their fundamental dissipation processes have been thoroughly studied^{11,27,28}, and their nonlinear vibrational response can be precisely tailored²⁹. As a consequence, it is possible to fabricate c-c beam resonators with a large detuning range³⁰ that facilitates the coupling between mechanical modes. In our study, we used a single crystalline silicon c-c beam to demonstrate the IR phenomenon. The natural frequency of the principal in-plane flexural mode, $f_{\text{in-plane}}$, is found to be 61.4 kHz through electrostatic actuation and detection, with a linear damping rate $\gamma_1/2\pi = 0.50$ Hz, corresponding to a quality factor (Q) of 122680 (Fig. 1a). When the in-plane motion is driven with increased actuation, the large transverse amplitude leads to non-negligible elongation of the beam, causing the restoring force to vary nonlinearly with the displacement³⁰. This well-known Duffing nonlinearity shifts the resonant frequency upward with increasing actuation, as shown in Fig. 1b. In this case, the resonant frequency (f_{res}) corresponds to the value where the vibrational amplitude peaks as the drive frequency is swept up. For a Duffing nonlinear resonator, the increase of the resonant frequency scales quadratically with the actuation, or equivalently, with v_{ac} in our setup (see Supplementary Information), as is shown in Fig. 1c. The resonant frequency increases quadratically with the driving strength until it reaches $f_{\text{IR}} = 64.9$ kHz, where it saturates due to the coupling of the principal mode with a higher frequency mode through an IR. This saturation frequency matches exactly one third of a higher frequency torsional mode of the same c-c beam,

whose thermomechanical noise spectrum (measured separately) is shown in Fig. 1d. The natural frequency of this torsional mode is $f_{\text{torsional}} = 194.6$ kHz, with a linear damping rate $\gamma_2/2\pi = 2.25$ Hz (corresponding to a Q of 86505). At this tuning condition, the higher frequency (torsional) mode drains mechanical energy from the principal mode via a nonlinear inter-modal coupling mechanism: instead of building a larger flexural in-plane mode, the energy input at frequency f_{IR} is used to excite the torsional mode at a frequency three times larger than f_{IR} (1:3 mode coupling).

In order to better understand the mechanism responsible for energy exchange and dynamic evolution of the IR, we put the resonator in a stationary oscillatory state through a closed-loop configuration, and then perform time-resolved measurements of its oscillation amplitude and frequency before and after the driving force is switched off (ringdown). We apply different self-sustaining schemes that allow the in-plane motion to reach autonomous oscillations whose frequency is determined by the mechanical resonance, which can be further tuned by the feedback force through either a phase-locked loop (PLL)⁹ or a feedback phase-delay^{31,32}. When the resonator's frequency is outside IR (i.e., in-plane oscillation frequency different from 64.9 kHz), the energy decay mechanism is typical of a single mode nonlinear oscillator³³: after the excitation is turned off, the amplitude immediately starts to decay towards zero, and the frequency decays toward the natural frequency of the principal in-plane flexural mode, $f_{\text{in-plane}}$ (Fig. 2a and 2b). The amplitude decay is well approximated by a simple exponential decay, with a dissipation rate of 0.68 Hz (Fig. 2a, inset). This dissipation rate is larger than the value obtained from quasi-static frequency sweep (Fig. 1a) due to other nonlinear processes dominant at large amplitudes³³ and frequency fluctuations¹⁰. The temporal evolution of the instantaneous frequency during ringdown,

obtained by performing fast Fourier transform (FFT) on the time-domain data, (Fig. 2b), clearly shows that the instantaneous frequency also decays from its initial value (63.6 kHz) towards the natural frequency of the principal in-plane flexural mode (61.4 kHz). The decay is also approximately exponential, with a decay rate of 1.39 Hz, i.e. twice that of the amplitude, as expected for a Duffing nonlinearity (see Supplementary Information). When the system is brought into IR as the in-plane oscillation frequency approaches 64.9 kHz, we find an unexpected and qualitatively different ringdown behavior: after the external excitation is removed, the amplitude and frequency of the in-plane motion remain constant for a certain period of time t_{coherent} (Fig. 2c and 2d). During t_{coherent} , the resonator continues oscillating with a stable sinusoidal waveform as if the external energy supply were still on (Fig. 2e). In other words, it behaves as an ideal autonomous oscillator that requires neither the external sustaining feedback circuitry for power supply nor a frequency reference. Beyond t_{coherent} , the principal mode resumes the expected exponential decay, both in terms of amplitude and frequency, as in a single mode nonlinear oscillator³³. Figure 2f shows the dependence of t_{coherent} on the actuation force, v_{ac} in our setup, suggesting a practical method to control the period of time where the in-plane mode does not decay.

A simple theoretical description of the results described in Fig. 2 can be obtained by modeling the IR condition through a 1:1 coupling of the principal nonlinear Duffing mode with a linear oscillator representing the higher frequency mode. In this case, the equations of motion for the two coupled modes are:

$$\begin{aligned}\ddot{x}_1 + \gamma_1 \dot{x}_1 + x_1 + \beta x_1^3 &= Jx_2 + F_{\text{fb}}, \\ \ddot{x}_2 + \gamma_2 \dot{x}_2 + \Omega_2^2 x_2 &= J'x_1,\end{aligned}\tag{1}$$

where γ_1, γ_2 are the dissipation rates for the respective modes, β is the Duffing nonlinear coefficient, and $\Omega_2 \gtrsim 1$ is the normalized frequency of mode x_2 . The modes x_1 and x_2 are linearly coupled to each other, with coupling coefficients J and J' . Only mode x_1 is driven by an external feedback force F_{fb} , to compensate the energy dissipation and achieve self-sustaining oscillations. For a positive Duffing coefficient, $\beta > 0$, the oscillation frequency of mode x_1 , Ω_1 , can be tuned up from its natural frequency (normalized to 1) by increasing F_{fb} . Without inter-modal coupling ($J = J' = 0$), the coupled system reduces to two independent modes, with mode x_2 asymptotically at rest, and mode x_1 behaving as a self-sustaining nonlinear oscillator with tunable frequency³² (see Supplementary Information). For finite linear coupling, mode x_2 can now be excited due to the motion of mode x_1 . When the oscillation frequency of mode x_1 coincides with that of mode x_2 , the IR condition is achieved and mode x_2 is then driven resonantly with strength determined by the coupling J' .

The stationary solutions to equation (1) determine the possible initial conditions of the ring-down evolution which, in turn, is governed by the same equations but with $F_{fb} = 0$. For the case where both modes have small dissipation rates ($\gamma_1, \gamma_2 \ll 1$), we can apply a perturbation method to solve Eq. (1), for both the steady state and the transient response during ringdown^{31,34} (see Supplementary Information). Figure 3 shows the numerical solutions of equation (1) for small dissipation ($\gamma_1, \gamma_2 \sim 10^{-5}$), sufficiently large Duffing nonlinear coefficients ensuring that the principal mode amplitude is well within the nonlinear regime ($\beta \sim 10^{-3}$ to 10^{-2}), and large coupling coefficients ($J \times J' \sim 10^{-9}$ to 10^{-7}). The time-resolved energy decay of the principal mode is plotted in Fig. 3a, and is compared with the decay of the nonlinear resonator outside IR. The simplified

model presented above qualitatively reproduces the experimental results of Fig. 2: at IR and for a finite period of time, t_{coherent} , the principal mode continues oscillating with practically constant amplitude (Fig. 3a) and frequency (Fig. 3b) after the external energy supply has been switched off. Figure 3c shows the accompanying time evolution of the higher frequency mode, indicating a rapid, non-exponential decay in its amplitude reaching toward zero at time t_{coherent} . These results indicate a net transfer of energy from the higher frequency mode to the principal mode, since the former decays at a rate much faster than the exponential decay rate characteristic of energy dissipation toward the environmental thermal bath (dotted line in Fig. 3c). The difference between the two curves in Fig. 3c provides a direct estimation of the amount of energy transfer from mode x_2 to mode x_1 during the period t_{coherent} . It clearly shows that a significant amount of the energy gets redirected toward mode x_1 instead of being dissipated to the environmental bath. For times longer than t_{coherent} , the amplitude of the higher frequency mode approaches zero, and the principal mode begins its exponential decay toward equilibrium. For the particular case of our experiment, with a 1:3 mode coupling between a flexural in-plane mode and a torsional mode, the torsional (higher frequency) mode acts as an energy reservoir for the flexural in-plane (principal) mode, by storing mechanical energy during the stationary state and transferring it back when the external feedback force is switched off.

A closer look to the time dependence of the principal mode amplitude during t_{coherent} shows coherent oscillations around its steady state value, with a relatively very small amplitude ($\sim 0.1\%$) and a slowly decreasing frequency (Fig. 3d). Furthermore, the phase difference between the two modes, η , whose value is constant before ringdown, presents similar oscillations that indicates a

oscillating flow of energy between the two modes (Fig. 3e). The simulated transient responses of η shows that it oscillates around a positive value, which implies that, despite the instantaneous direction of energy flow, there is a net energy flow from mode x_2 to mode x_1 . Consequently, the amplitude of mode x_2 decays rather abruptly, while the amplitude of mode x_1 , remains - on the average - practically constant. This dynamical exchange breaks down as soon as mode x_2 exhausts its energy, and from then on, mode x_1 behaves as a single mode nonlinear oscillator.

While our experimental setup cannot directly measure the coherent amplitude oscillations shown in Fig. 3d due to the limitation of the measurement bandwidth, we do see their presence in the time-resolved frequency spectrum before and during t_{coherent} . Figure 4 shows the temporal evolution of the resonator's frequency as it transits from steady-state to ringdown in a device that is driven to a strong IR condition with larger feedback force F_{fb} . During steady-state we find two sidebands flanked around the main peak in the power spectrum (regime I), that during t_{coherent} (regime II), both sidebands evolve towards the frequency of the principal in-plane flexural mode, merging with it at $t = t_{\text{coherent}}$. When the frequency of mode x_1 is exponentially decaying (regime III), there is no evidence of sidebands because there is no coupling between the vibrational modes and thus no exchange of energy. The emergence of these sidebands is a direct consequence of the energy change (cf. Fig. 3e), whose value quantifies the exchange rate γ_{ex} . For the particular case presented in Fig. 4a, we obtained a $\gamma_{\text{ex}} \sim 800$ Hz, which is almost three orders of magnitude larger than the intrinsic damping rate of each of the coupled modes (~ 1 Hz). By performing similar frequency measurements at different driving forces, a linear correlation between t_{coherent} and γ_{ex} is obtained (Fig. 4a, right inset). The data indicates that a $\gamma_{\text{ex}} > 200$ Hz is needed in order to have a

finite t_{coherent} and the larger the γ_{ex} , the larger the t_{coherent} .

The experimental and numerical results discussed above demonstrate that mode coupling can be used to engineer the intrinsic relaxation phenomena of nonlinear oscillators. In particular, when different vibrational modes are coupled through an IR, the exchange of energy between modes could happen orders of magnitude faster than the exchange of energy with the external environmental bath (Fig. 4b). Under these conditions, nonlinear resonators can sustain, for a finite period of time, stable oscillations without external energy supply. The dissipation engineering concept presented in this work could be applied to a wide range of MEMS and NEMS oscillators whose performance is limited by the electrical noise in the feedback circuit³⁵. MEMS and NEMS resonators oscillating without external power should be ideal devices to identify the ultimate stability limit imposed by thermomechanical noise³⁶. The possibility to control the energy exchange rate between coupled modes creates a testbed to validate theories of thermalization of nonlinear systems out of equilibrium^{37,38} and resonant nonlinear friction³⁹. In atomically thin NEMS resonators, where the nonlinear dynamic response can be easily achieved⁴⁰, mode coupling can have a significant effect on the relaxation process toward equilibrium⁴¹.

It is worthwhile emphasizing the manifold role of nonlinearity in the occurrence of the phenomena studied here. In the first place, nonlinearity is responsible for the coupling between different oscillation modes, enabling the exchange of energy that determines their mutual influence. At the same time, the upshift of the oscillation frequency as the driving force increases in amplitude makes it possible that the nonlinear oscillator reaches the condition of IR - an effect which is absent

in harmonic oscillators. Finally, the presence of an interval of coherence just after the driving force is switched off has also to be ascribed to nonlinearity. The combination of beating and exponential decay that characterizes the dynamics of coupled *linear* oscillators is in fact not able to account for such temporary stability of the oscillation amplitude in the absence of an external action.

References

1. Razavy, M. *Classical and quantum dissipative systems* (World Scientific, 2005).
2. Braginsky, V. B., Mitrofanov, V., Panov, V. I. & Eller, C. *Systems with small dissipation* (University of Chicago Press, 1985).
3. Chaste, J. *et al.* A nanomechanical mass sensor with yoctogram resolution. *Nature Nanotechnology* **7**, 301–304 (2012).
4. Decca, R., López, D., Fischbach, E. & Krause, D. Measurement of the casimir force between dissimilar metals. *Physical review letters* **91**, 050402 (2003).
5. Audoin, C. & Guinot, B. *The measurement of time: time, frequency and the atomic clock* (Cambridge University Press, 2001).
6. van Beek, J. T. M. & Puers, R. A review of mems oscillators for frequency reference and timing applications. *Journal of Micromechanics and Microengineering* **22**, 013001 (2012).
7. O’Connell, A. D. *et al.* Quantum ground state and single-phonon control of a mechanical resonator. *Nature* **464**, 697–703 (2010).
8. Aspelmeyer, M., Kippenberg, T. J. & Marquardt, F. *Cavity optomechanics: nano-and micromechanical resonators interacting with light* (Springer, 2014).
9. Antonio, D., Zanette, D. H. & López, D. Frequency stabilization in nonlinear micromechanical oscillators. *Nature communications* **3**, 806 (2012).

10. Dykman, M. *Fluctuating nonlinear oscillators: from nanomechanics to quantum superconducting circuits* (OUP Oxford, 2012).
11. Cleland, A. N. *Foundations of nanomechanics: from solid-state theory to device applications* (Springer Science & Business Media, 2013).
12. Okamoto, H., Mahboob, I., Onomitsu, K. & Yamaguchi, H. Rapid switching in high-q mechanical resonators. *Applied Physics Letters* **105**, 083114 (2014).
13. Ford, J. E., Aksyuk, V. A., Bishop, D. J. & Walker, J. A. Wavelength add-drop switching using tilting micromirrors. *Journal of lightwave technology* **17**, 904 (1999).
14. Abbott, B. *et al.* Observation of gravitational waves from a binary black hole merger. *Physical review letters* **116**, 061102 (2016).
15. Wilson, D., Regal, C., Papp, S. & Kimble, H. Cavity optomechanics with stoichiometric silicon films. *Physical review letters* **103**, 207204 (2009).
16. Norte, R. A., Moura, J. P. & Gröblacher, S. Mechanical resonators for quantum optomechanics experiments at room temperature. *Physical review letters* **116**, 147202 (2016).
17. Reinhardt, C., Müller, T., Bourassa, A. & Sankey, J. C. Ultralow-noise silicon trampoline resonators for sensing and optomechanics. *Physical Review X* **6**, 021001 (2016).
18. Teufel, J. *et al.* Sideband cooling of micromechanical motion to the quantum ground state. *Nature* **475**, 359–363 (2011).

19. Singh, V. *et al.* Optomechanical coupling between a multilayer graphene mechanical resonator and a superconducting microwave cavity. *Nature nanotechnology* **9**, 820–824 (2014).
20. Weis, S. *et al.* Optomechanically induced transparency. *Science* **330**, 1520–1523 (2010).
21. Eichenfield, M., Chan, J., Camacho, R. M., Vahala, K. J. & Painter, O. Optomechanical crystals. *Nature* **462**, 78–82 (2009).
22. Mahboob, I., Nishiguchi, K., Okamoto, H. & Yamaguchi, H. Phonon-cavity electromechanics. *Nature Physics* **8**, 387–392 (2012).
23. Manevich, A. I. & Manevich, L. I. *The mechanics of nonlinear systems with internal resonances* (World Scientific, 2005).
24. Nayfeh, A. H. & Mook, D. T. *Nonlinear oscillations* (John Wiley & Sons, 2008).
25. Cottone, F., Vocca, H. & Gammaitoni, L. Nonlinear energy harvesting. *Physical Review Letters* **102**, 080601 (2009).
26. Cao, D., Leadenham, S. & Erturk, A. Internal resonance for nonlinear vibration energy harvesting. *The European Physical Journal Special Topics* **224**, 2867–2880 (2015).
27. S. Timoshenko, W. W., D. H. Young. *Vibration Problems in Engineering* (New York, Wiley, 1974).
28. Ghaffari, S. *et al.* Accurate modeling of quality factor behavior of complex silicon mems resonators. *Journal of Microelectromechanical Systems* **24**, 276–288 (2015).

29. Dou, S., Strachan, B. S., Shaw, S. W. & Jensen, J. S. Structural optimization for nonlinear dynamic response. *Phil. Trans. R. Soc. A* **373**, 20140408 (2015).
30. Lifshitz, R. & Cross, M. C. Nonlinear dynamics of nanomechanical and micromechanical resonators. In *Reviews of Nonlinear Dynamics and Complexity*, 1–52 (Wiley-VCH Verlag GmbH & Co. KGaA, 2009).
31. Arroyo, S. I. & Zanette, D. H. Duffing revisited: phase-shift control and internal resonance in self-sustained oscillators. *The European Physical Journal B* **89**, 1–8 (2016).
32. Chen, C., Zanette, D. H., Guest, J. R., Czaplewski, D. A. & López, D. Self-sustained micromechanical oscillator with linear feedback. *Physical Review Letters* **117**, 017203 (2016).
33. Polunin, P. M., Yang, Y., Dykman, M. I., Kenny, T. W. & Shaw, S. W. Characterization of mems resonator nonlinearities using the ringdown response. *Journal of Microelectromechanical Systems* **25**, 297–303 (2016).
34. Nayfeh, A. H. *Perturbation methods* (John Wiley & Sons, 2008).
35. Feng, X. L., White, C. J., Hajimiri, A. & Roukes, M. L. A self-sustaining ultrahigh-frequency nanoelectromechanical oscillator. *Nature Nanotechnology* **3**, 342–346 (2008).
36. Sansa, M. *et al.* Frequency fluctuations in silicon nanoresonators. *Nature nanotechnology* **11**, 552–558 (2016).
37. Dykman, M. Theory of nonlinear nonequilibrium oscillators interacting with a medium. *Zh. Eksp. Theor. Fiz* **68**, 2082–2094 (1975).

38. Midtvedt, D., Croy, A., Isacsson, A., Qi, Z. & Park, H. S. Fermi-pasta-ulam physics with nanomechanical graphene resonators: Intrinsic relaxation and thermalization from flexural mode coupling. *Physical review letters* **112**, 145503 (2014).
39. Shoshani, O., Shaw, S. & Dykman, M. Resonant nonlinear friction in coupled vibrational systems. *unpublished* .
40. Chen, C. & Hone, J. Graphene nanoelectromechanical systems. *Proceedings of the IEEE* **101**, 1766–1779 (2013).
41. Guttinger, J. *et al.* private communications. *unpublished* .

Acknowledgements The authors like to thank Mark Dykman, Jeffrey Guest, Aftab Ahmed, Ori Shoshani, Pavel Polunin, Thomas Kenny, Adrian Bachtold, Andreas Isacson, and Vladimir Aksyuk for critical discussions. Use of the Center for Nanoscale Materials at the Argonne National Laboratory was supported by the U.S. Department of Energy, Office of Science, Office of Basic Energy Sciences, under Contract No. DE-AC02-06CH11357. S.S. is supported by NSF grant 1561829 and funds from Florida Institute of Technology.

Competing Interests The authors declare that they have no competing financial interests.

Author contributions C.C., D.C. and D.L. conceived and designed the experiments, C.C. and D.C. performed the experiments and analyzed the data, D.H.Z., S.S. and C.C. performed the modeling and numerical simulations, C.C. and D.L. co-wrote the paper. All authors discussed the results and commented on the manuscript.

Correspondence Correspondence and requests for materials should be addressed to D.L. (email: dlopez@anl.gov).

Fig. 1

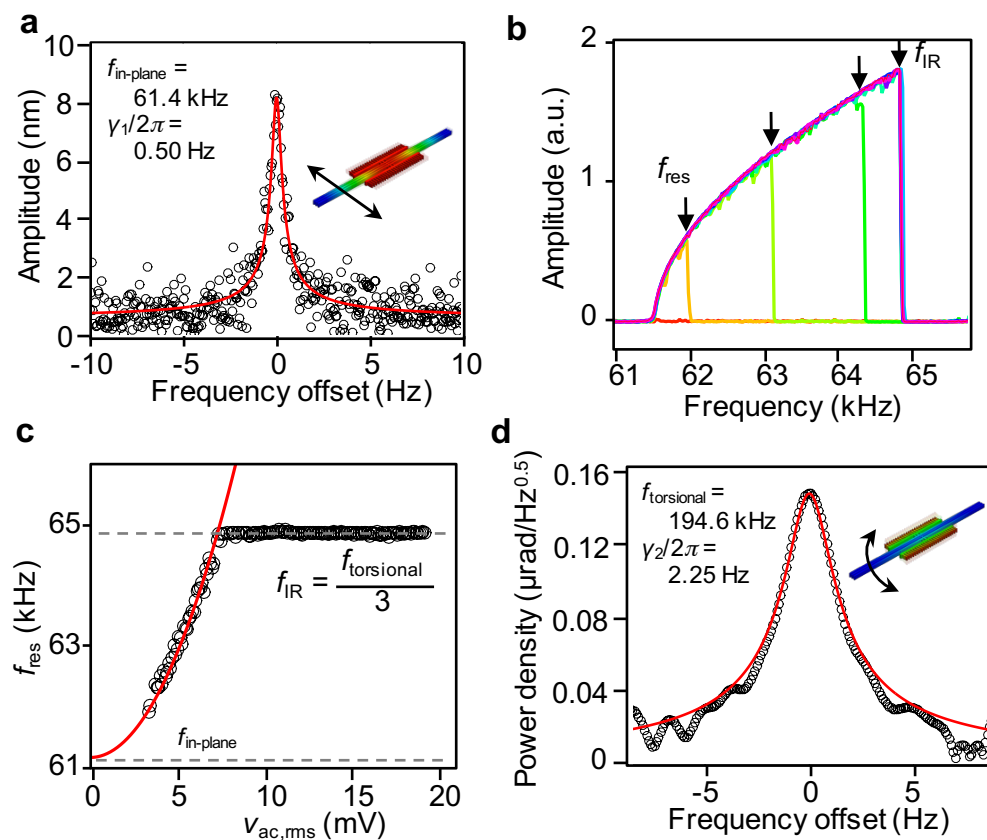


Fig. 2

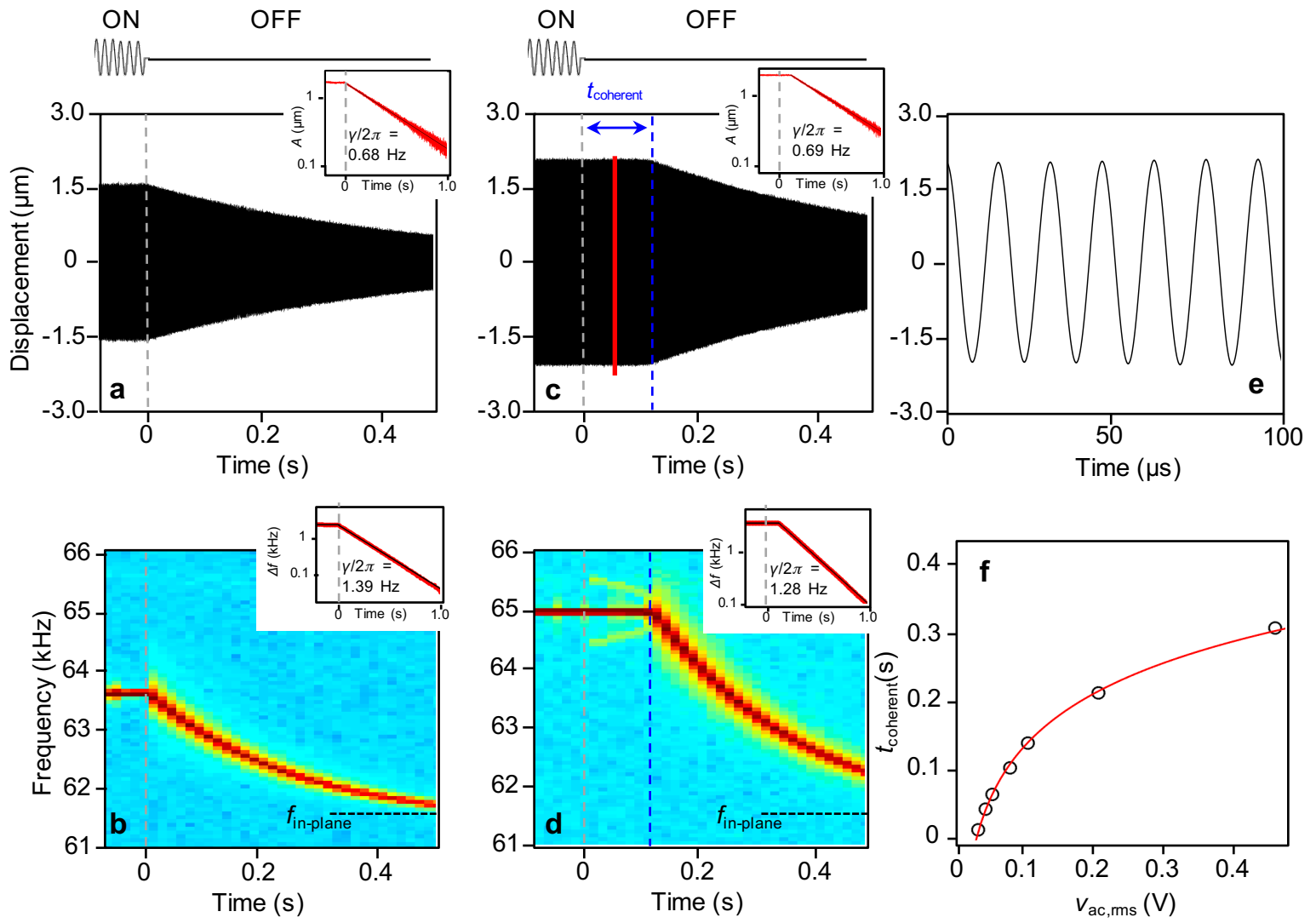


Fig. 3

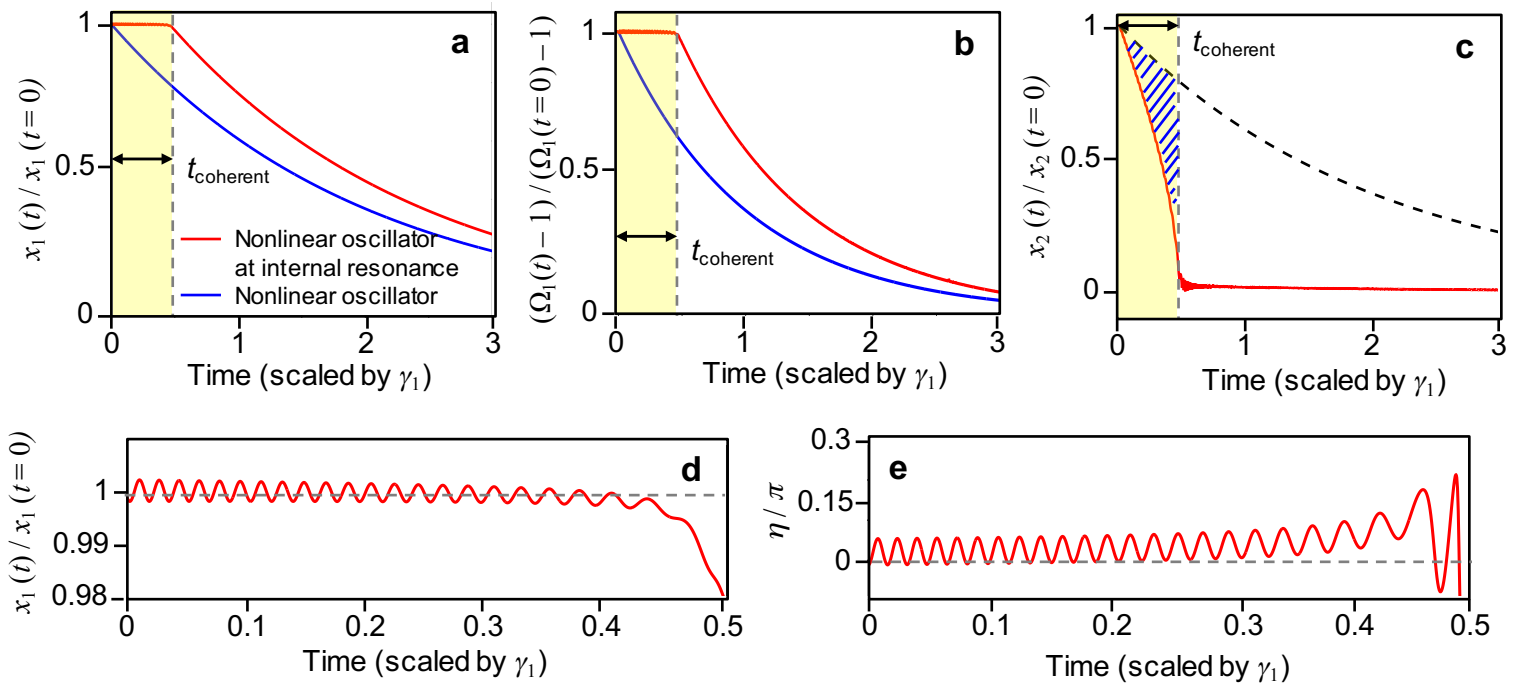


Fig. 4

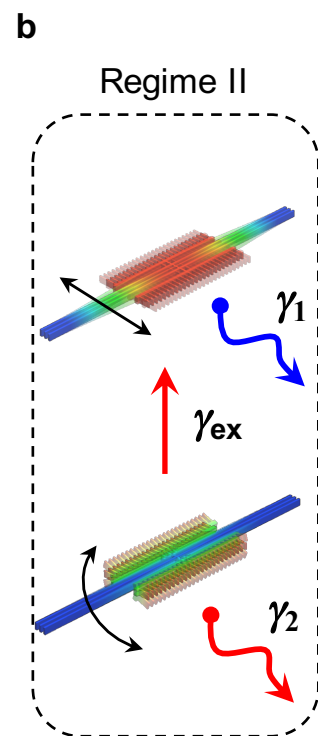
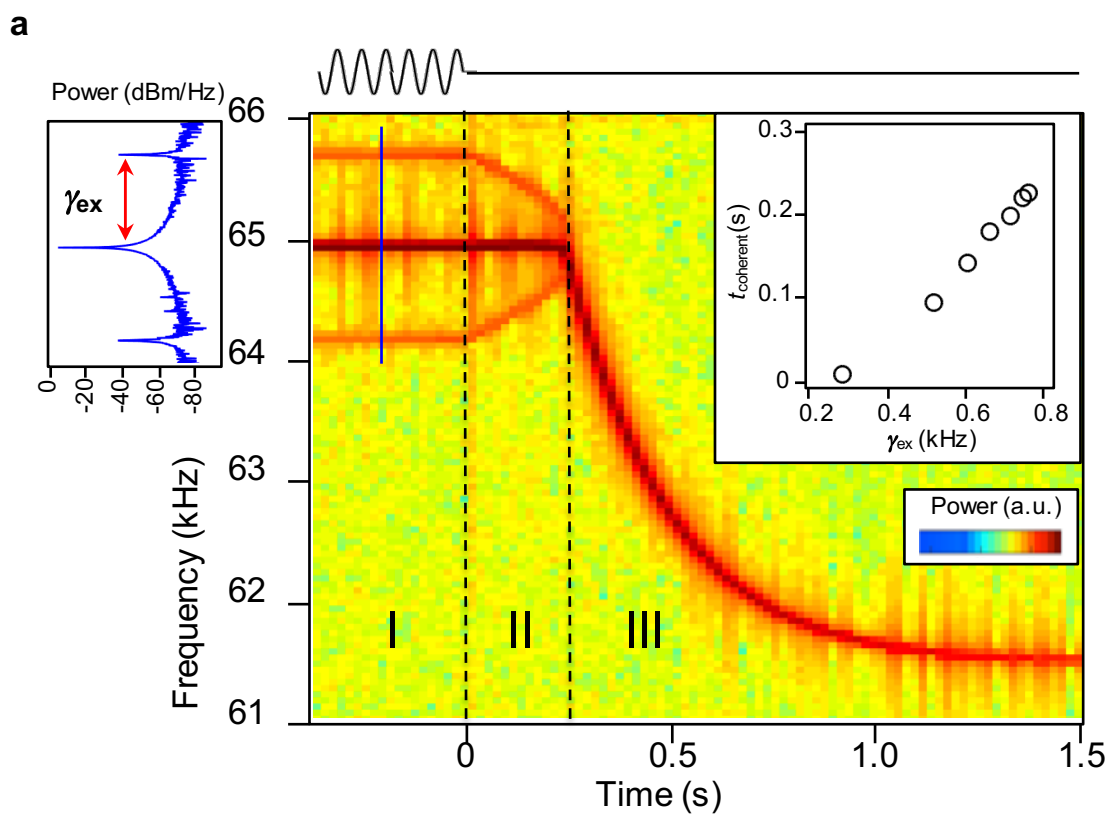


Figure 1 Internal resonance (IR) in a nonlinear MEMS oscillator. **a.** Linear resonance of the in-plane oscillation mode measured with open-loop setup, DC bias $V_{DC} = 7$ V, and alternating current (ac) voltage actuation $v_{ac} = 40 \mu\text{V}$. Inset: finite element simulation of the in-plane mode shape (CoventorWare). The length and thickness of the c-c beam are $500 \mu\text{m}$ and $10 \mu\text{m}$, respectively. The central portion consists of 3 parallel beams, each with width of $3 \mu\text{m}$. **b.** The vibrational amplitude of the in-plane motion as the external excitation frequency is swept up (open-loop), with excitation amplitude v_{ac} increasing from 1 to 19 mV at 2 mV steps. At large v_{ac} , the vibrational amplitude spectrum shows an asymmetrical line-shape that skews towards high frequencies, due to the positive Duffing nonlinearity. As v_{ac} increases, the frequency at which the vibrational amplitude peaks, f_{res} , also increases, until reaching 64.9 kHz. **c.** Measured f_{res} with different v_{ac} . For $v_{ac} \lesssim 7.5$ mV, f_{res} follows a quadratic dependence on v_{ac} . For $v_{ac} \gtrsim 7.5$ mV, f_{res} stabilizes at 64.9 kHz, which equals to one third of $f_{torsional}$. Notice that all the voltages are rms values. **d.** Thermomechanical noise spectrum of the torsional mode measured with optical interferometry (see Supplementary Information for details).

Figure 2 Ringdown responses outside and inside IR. **a.** Oscillation displacement of the in-plane mode before and after the external drive is turned off (at time equals 0 sec), when its oscillation frequency is outside the IR condition. The inset shows the extracted envelope of the displacement, plotted in logarithmic scale. The black line is a fit with an exponential decay, with a decay rate of 0.68 Hz. The external excitation v_{ac} is 6.3 mV. **b.** Temporal frequency response of the oscillation during the same period of time.

The power spectrum at each nominal time t_i is obtained by performing a nonoverlapping fast Fourier transform of the time domain data in a narrow window of 16 ms around t_i . The inset shows the extracted instantaneous frequency offset from the principle in-plane frequency, with fitting an to exponential decay (black line). The fitted decay rate is 1.39 Hz. **c.** Oscillation displacement of the in-plane mode before and after the external drive is turned off, when its oscillation frequency is inside the IR condition. For the first 108 ms after the ringdown starts, the envelope of the oscillation remains practically constant. The inset shows the extracted oscillation envelop during ringdown, with an exponential decay fit for the $t > t_{\text{coherent}}$ portion. **d.** Temporal frequency response of the oscillation during the same period of time, showing constant frequency oscillations during t_{coherent} . The inset shows the extracted instantaneous frequency offset from the principle in-plane frequency, with fitting to an exponential decay (black line) for the $t > t_{\text{coherent}}$ portion. The fitted decay rate is 1.28 Hz. For $t < 0$, the self-sustaining motion is driven by an external PLL that outputs a single-frequency signal. For $t \in (0, t_{\text{coherent}})$ the transient response is only controlled by the system dynamics and two sidebands flanking the main frequency peak appear (see main text and Supplementary Information for details). **e.** Zoomed-in view of the oscillation of ringdown of **c**, indicating clean and stable sinusoidal oscillations (the time is offset to 50 ms). **f.** t_{coherent} obtained with different steady-state drive v_{ac} . The red line is a theoretical fit with the model described in Equation (1) (see Supplementary Information for details).

Figure 3 Modeling the ringdown response of a nonlinear oscillator. a. Simulated

transient responses of the vibrational amplitude decay (i.e. envelope of the oscillation displacement) of a single mode nonlinear oscillator (blue) and a nonlinear oscillator at internal resonance (red). Note that for the nonlinear oscillator at IR, the vibrational amplitude does not decay during t_{coherent} after the external excitation is removed at $t = 0$.

b. Simulated transient responses of the instantaneous frequency offset, $\Omega_1 - 1$, for the two cases presented in **a**. After the external excitation is removed, the instantaneous frequency for the single mode nonlinear oscillator (blue) decays exponentially towards zero, while for the nonlinear oscillator at IR (red), the instantaneous frequency stays constant.

c. Temporal evolution during ringdown of the higher frequency mode x_2 at IR: the amplitude (red line) decays much faster than the expected exponential decay (dashed black line), indicating faster energy transfer to mode x_1 than to the environmental bath. The shaded area indicates the amount of energy transferred from mode x_2 to mode x_1 .

d. Time dependence of the principal mode (x_1) amplitude during the period t_{coherent} , revealing small oscillations (~ 0.1 %) around its initial value, with a decreasing frequency.

e. Simulated phase difference η between the two coupled modes during the same period of time as in **d**. It shows the presence of coherent oscillations around a positive average value of η , indicating a net energy transfer from mode x_2 to mode x_1 .

Figure 4 Time scale of the energy exchange dynamic at IR. **a.** Temporal evolution of the instantaneous frequency before (regime I) and during (regime II and III) ringdown. For $t < 0$, the self-sustaining motion is driven by a linearly feedback signal with appropriate phase-delay, instead of using a PLL setup as the one used to obtain the data presented

in Figure 2. In regime I, there are two sidebands flanking the main steady-state frequency (64.9 kHz, IR) that indicate the energy exchange rate between the main and higher frequency modes (a single power spectrum is shown in left inset). During t_{coherent} (regime II), the main frequency stays constant and the sidebands merge toward the main frequency peak, and finally disappear at the end of regime II. Regime III represents the normal decay for a single mode nonlinear oscillator and thus shows no evidence of sidebands. Right inset: extracted γ_{ex} plotted against corresponding t_{coherent} , showing a linear correlation between them. **b.** Schematic representation of the energy flow during t_{coherent} (regime II): there is a net energy flow from the high frequency torsional mode to the in-plane principal mode at a rate $\gamma_{\text{ex}} \gg \gamma_1, \gamma_2$. This large difference in relaxation rates causes the in-plane principal mode to maintain stable oscillations even after the external power supply has been switched off.